







Polariton-assisted long-distance energy transfer between excitons in two-dimensional semiconductors

Tuomas Pajunpää ¹, Fedor Nigmatulin ¹, Suvi-Tuuli Akkanen ¹, Henry Fernandez ^{1,*},
Gerrit Groenhof ² and Zhipei Sun ^{1,†}

¹*QTF Centre of Excellence, Department of Electronics and Nanoengineering, Aalto University, FI-00076 Aalto, Finland*

²*Nanoscience Center, Department of Chemistry, P.O. Box 35, FI-40014 University of Jyväskylä, Finland*



(Received 5 January 2024; revised 9 April 2024; accepted 11 April 2024; published 3 May 2024)

Strong exciton-photon coupling offers an effective path for polariton-mediated long-distance coherent energy transfer (ET) between excitonic states. Here, we demonstrate strong coupling between excitons in WS₂ monolayers, MoS₂ bilayer, and photons in a tunable optical microcavity at room temperature. Full quantum dynamics simulations based on experimental parameters show that the demonstrated system provides an efficient and adjustable platform for ultrafast polariton-assisted ET between the excitons in two-dimensional materials when the separation between them exceeds 1 μm.

DOI: [10.1103/PhysRevB.109.195409](https://doi.org/10.1103/PhysRevB.109.195409)

I. INTRODUCTION

Energy transfer (ET) between quantum emitters (QEs) will play a pivotal role in future quantum devices in such promising fields as quantum computing [1,2] and networks [3]. To achieve the level of real applications, it is highly desirable to obtain stable and controllable qubits which can exchange energy. Excitons in molecules or low-dimensional materials are promising implementations of QEs that can be used in a wide range of quantum technologies. ET between excitons can emerge if they are coupled by interactions, such as nonradiative resonant transfer through dipole-dipole coupling. Such ET processes have been classically treated only as short-distance interactions, limited by the Förster distance of ~10 nm [4,5]. Recent progress in cavity quantum electrodynamics has increased the ET distance in strong coupling microcavities, where the excitons are coupled to a common cavity photon mode. The out-of-plane delocalization of polariton states based on the micrometer scale of its coherence length [6] allows excitons to overcome the spatial separation, enhancing ET over distances well beyond the Förster coupling limit [7,8]. Thus, polariton-assisted ET is an intriguing research direction because it opens up opportunities for efficient manipulation of energy at the nanoscale.

Experimental observations of long-distance ET mediated by polaritons have been reported in quantum wells (QWs) [9] and organic semiconductors [10]. Both studies achieved an ET distance of ~2 μm, exceeding the Förster distance over a hundredfold. However, both QWs and organic semiconductors exhibit essential limitations restricting their potential for nanotechnology applications: Structures based on traditional semiconductors suffer either from low exciton binding energies or inefficient charge injection, limiting practical use to cryogenic temperatures [11]; some organic semiconductors

can support room temperature (RT) exciton-polaritons, but photobleaching degrades the chemical stability of molecules impairing the durability of previously demonstrated materials over extended periods of time [12]. Additionally, challenges in fabrication of organic semiconductor thin films with consistent optical properties limits the practical reproducibility of such devices. Thereby, there is a continuous demand for stable materials with large exciton binding energies that can support polaritons at RT in nanotechnology applications.

Transition metal dichalcogenides (TMDs) contain a group of layered semiconductor materials that exhibit exciton transitions with large binding energies (up to 1.0 eV [13]) and tunable charge carrier injection [14], thus supporting polaritons in microcavities at RT [15,16]. Such properties can be observed even at the monolayer limit, potentially exhibiting ~100% quantum yield in the photoluminescence process [17]. The versatile characterization and fabrication methods of TMDs allow accurate control of layer count and rotation angle, allowing their consistent fabrication and nanodevice integration. The result is a higher level of device reproducibility than in organic semiconductors. Although these materials present challenges in their chemical stability, they can be coated with thin, highly stable dielectric layers, extending the lifetime of nanodevices [18,19]. Among semiconducting TMDs, tungsten disulfide (WS₂) and molybdenum disulfide (MoS₂) exhibit exciton transitions with energy loss factors suitable for RT polaritons in microcavities [15,20]. Although conventional Förster-limited ET has already been demonstrated between WS₂ monolayers separated by a thin dielectric layer [21], long-distance ET still has not been achieved.

In this paper, we investigate polariton-mediated RT ET between excitons in WS₂ and MoS₂ over a long-distance range through experimental data analyzed by quantum mechanical simulations that use experimental values as inputs. The studied system consists of a WS₂/hBN/WS₂ heterostructure and a MoS₂ bilayer placed inside a tunable Fabry-Pérot microcavity which allows sweeping low order resonant modes with a precision of ~7 meV. Strong exciton-photon coupling

*henryfernandez09@live.com

†zhipei.sun@aalto.fi

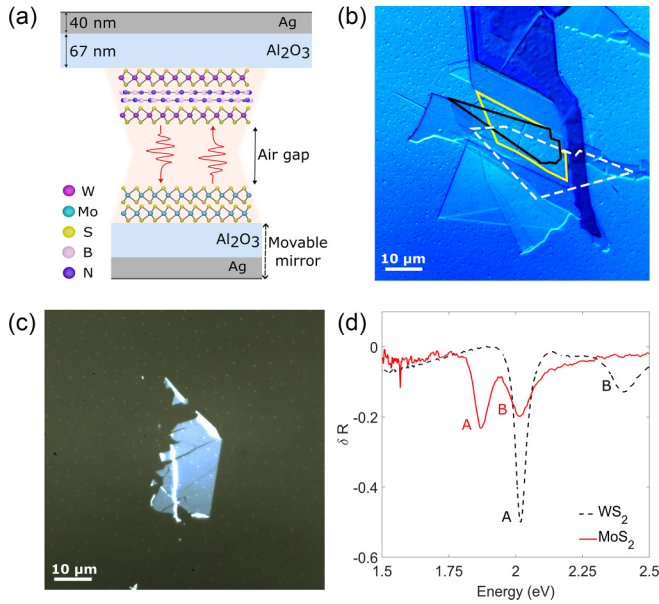


FIG. 1. Sample configuration presented by an illustration, optical images, and reflection spectra of the components. (a) Schematic of the sample and cavity configuration. (b) Differential interference contrast image of two WS_2 monolayers [black and yellow (light gray) continuous lines] with a hBN layer intercalated in between (white dashed line). (c) Optical microscopy image of the MoS_2 bilayer flake. (d) Reflection spectra of the WS_2 (black dashed line) and MoS_2 (red solid line) flakes. The labels A and B represent the respective excitons of the materials.

of both materials is confirmed by an anticrossing feature in transmission spectra as a function of the cavity length, and occurs when the air gap between mirrors is nearly $1 \mu\text{m}$. Fully quantum mechanical simulations of exciton population dynamics show the pronounced maximum of the energy exchange between considered excitons in time and frequency domains. The possibility to tune the resonant frequency of the cavity gives us an additional degree of freedom to manipulate polariton-assisted coherent ET. In this paper, we propose that the demonstrated system can be an experimentally accessible platform for efficient long-distance ET at RT. The results of this paper are a step toward a wide range of future applications, such as quantum technologies.

II. SAMPLE

A schematic of the system is presented in Fig. 1(a). The system comprises a $\text{WS}_2/\text{hBN}/\text{WS}_2$ heterostructure placed on a cavity mirror and bilayer MoS_2 placed on the opposite mirror. The WS_2 heterostructure is formed by two monolayers of WS_2 separated by an intercalated hBN flake with a thickness of $\sim 2 \text{ nm}$ estimated by optical contrast. This heterostructure increases the coupling factor with cavity photons by a factor of 1.4 compared with a single WS_2 monolayer, without increasing the loss factor. The MoS_2 bilayer also increases the coupling strength by the same factor, with an increase of the loss factor that remains low enough so MoS_2 B excitons can be strongly coupled to cavity photons. The bilayer and heterostructure present a balanced trade-off between

loss minimization and a sufficiently large coupling strength for the realization of polaritons in the microcavity at RT [22].

Optical microscopy images of the fabricated flakes are shown in Fig. 1(b) (WS_2) and Fig. 1(c) (MoS_2). The flakes were obtained via mechanical exfoliation and then deterministically transferred onto the cavity mirrors using a micromanipulator tool [23]. The thickness of each layer of the heterostructures was estimated by the optical contrast [24]. Each cavity mirror consists of a 40 nm thick Ag film deposited on a Ti-coated glass substrate, with a Ti thickness of 3 nm. The silver films were coated with 67 nm of aluminum oxide that acts as a protection against oxidation, and it also allows for positioning the semiconductor materials at the antinode of the intracavity mode, maximizing the exciton-photon coupling. The three layers of Ag, Ti, and 5 nm Al_2O_3 films forming the mirrors were deposited in the same physical vapor deposition system under high vacuum conditions. The remaining Al_2O_3 was deposited by atomic layer deposition. See Appendix A for more details of the cavity structure.

Figure 1(d) shows the measured differential reflection spectra where we identify the A and B exciton transitions of the WS_2 and MoS_2 flakes. These measurements were performed on each flake separately when already placed onto a mirror. We compared the measured reflections of the silver mirror with and without the flake. The data were normalized by subtracting the reflection spectrum of the silver mirror, with both light on (reflection) and off (noise), from the reflection spectra of the flakes on silver. These spectra were fit with Gaussian curves to obtain the exciton decay rates from the peak widths, which were used as input values in the simulations presented later in this paper. It is worth mentioning that we do not consider the presence of dark excitons in the system since they are inaccessible in our experiments, and this is out of the scope of this paper on long-distance ET.

III. HOPFIELD COEFFICIENTS AND STRONG COUPLING

The exciton and photon contributions to the polariton bands are described by the Hopfield coefficients [25]. To determine the Hopfield coefficients experimentally, first, we measured the transmission spectra of the system as a function of the cavity length, followed by fitting polariton bands calculated by the coupled oscillator model to the measured data for every value of the cavity length. The coupling constants of the model are kept as fitting parameters, which we tune to the experimental data. Finally, we calculate eigenvalues of the fitted polariton bands, from which we obtain the Hopfield coefficients.

To fit the coupling matrix elements of the coupled oscillator model to the measured data accurately, the measured spectrum for each cavity length was fitted with one or two Gaussian peaks, depending on if the data had a visible peak splitting. The fitted central positions of Gaussian peaks are marked as red circles in Figs. 2(a) and 2(e). In these figures, we also include the uncoupled dispersion of excitons and cavity photons as white lines. The coupling constants were optimized to achieve a fit between the calculated polariton bands shown as dotted lines and the peak positions of the measured data [see Figs. 2(a) and 2(e)]. Following this procedure, we obtain coupling constants for MoS_2 A and B excitons from

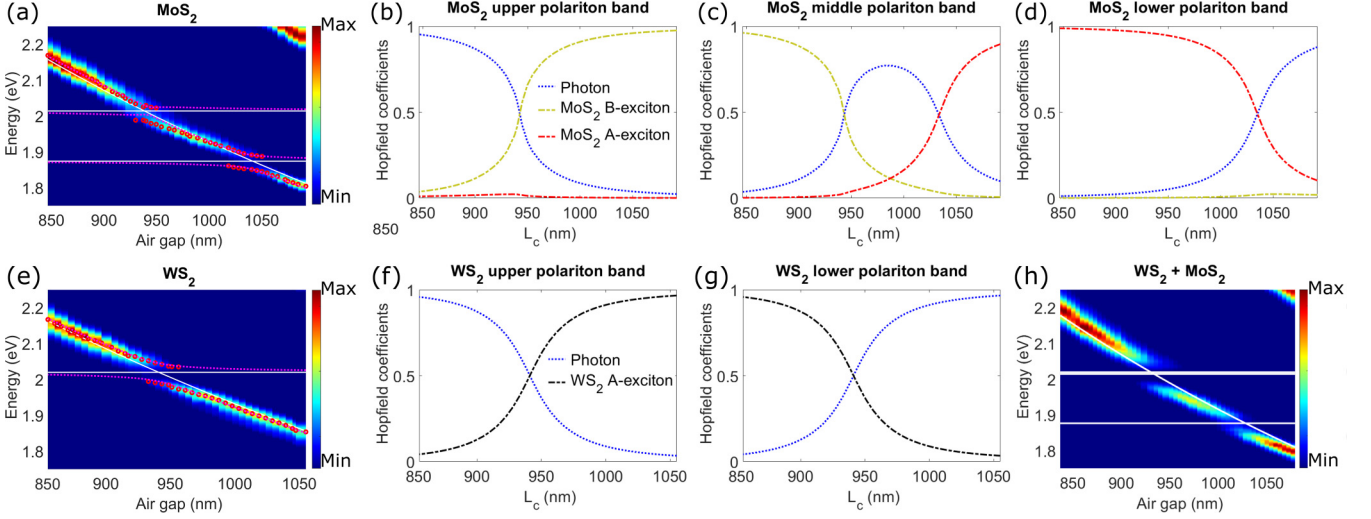


FIG. 2. Experimental cavity transmission spectra as a function of cavity length for (a) MoS₂ and (e) WS₂. Horizontal white lines are the free exciton frequencies, tilted white line is the empty cavity frequency, red circles are the Gaussian fit maxima for every spectrum, and dotted lines are the calculated polariton bands. Hopfield coefficients for MoS₂ (b) upper polariton band, (c) middle polariton band, and (d) lower polariton band, and for WS₂ (f) upper polariton band and (g) lower polariton band. (h) Transmission spectra as a function of cavity length for a cavity containing both WS₂ and MoS₂.

Fig. 2(a) and for the WS₂ A exciton from Fig. 2(e). From the fit in Fig. 2(a), we obtain Hopfield coefficients for upper, middle, and lower polariton bands of MoS₂ [Figs. 2(b)–2(d), respectively]. From the fit in Fig. 2(e), we obtain Hopfield coefficients for upper and lower polariton bands of WS₂ [Figs. 2(f)–2(g), respectively]. The coupling constants obtained through this procedure were used as input values in the exciton-photon population dynamics simulations. Finally, a measurement for a cavity containing both WS₂ and MoS₂ is presented in Fig. 2(h).

The strong coupling condition can be confirmed by clear anticrossings of WS₂ and MoS₂ excitons in Figs. 2(a) and 2(e) and supported by the strong coupling limit condition [26]:

$$2g > \frac{\gamma_{\text{ex}} + \gamma_c}{2}, \quad (1)$$

where g is the coupling factor, γ_{ex} is the decay rate of an exciton, and γ_c is the decay rate of a cavity. The parameters presented in Table I show that the strong coupling condition is satisfied for all three exciton transitions.

IV. THEORETICAL MODEL

A. Non-Hermitian Hamiltonian

Population dynamics of QEs in the resonant optical microcavity describe the energy exchange between the emitters in time. Here, we utilize the simplest two-level system (TLS) model as the description of the QE, which in our case is an

TABLE I. Experimental parameters of the cavity and excitons.

Exciton	g	γ_c (meV)	γ_{ex} (meV)	ω_{ex} (meV)
A-WS ₂	33	34	48	2019
A-MoS ₂	30	34	61	1876
B-MoS ₂	33	34	90	2021

exciton. Population dynamics of lossless TLSs can be treated in the framework of the time-dependent Schrödinger equation. For the consideration of dissipation in the open system, one can apply a non-Hermitian Hamiltonian with complex diagonal elements and obtain the analytical solution of the problem. For the system considered in this paper, the non-Hermitian Hamiltonian can be written as follows:

$$H = \hbar \begin{pmatrix} \omega_c - i\frac{\gamma_c}{2} & g_{e1A} & g_{e2A} & g_{e2B} \\ g_{e1A} & \omega_{1A} - i\frac{\gamma_{1A}}{2} & 0 & 0 \\ g_{e2A} & 0 & \omega_{2A} - i\frac{\gamma_{2A}}{2} & 0 \\ g_{e2B} & 0 & 0 & \omega_{2B} - i\frac{\gamma_{2B}}{2} \end{pmatrix}, \quad (2)$$

where ω_c is the frequency of the cavity photon; ω_{1A} , ω_{2A} , and ω_{2B} are the transition frequencies of the WS₂ A, MoS₂ A, and B excitons, respectively; g_{e1A} , g_{e2A} , and g_{e2B} denote coupling parameters between corresponding excitonic transitions and the cavity field; and \hbar is a reduced Planck constant. The benefits of this approach are the computational simplicity and, in some cases, the appearance of interesting features such as exceptional points [27]. At the same time, this approach fails at certain system parameters due to the non-hermicity, as described in Appendix B.

B. Lindblad master equation

A lossless system of three TLS excitons in the optical cavity also can be considered with the Tavis-Cummings model for the one-mode field [28]:

$$H = \hbar\omega_c a^\dagger a + \hbar\omega_{e1A} \sigma_{e1A}^+ \sigma_{e1A}^- + \hbar\omega_{e2A} \sigma_{e2A}^+ \sigma_{e2A}^- + \hbar\omega_{e2B} \sigma_{e2B}^+ \sigma_{e2B}^- + \hbar g_{e1A} (a \sigma_{e1A}^+ + a^\dagger \sigma_{e1A}^-) + \hbar g_{e2A} (a \sigma_{e2A}^+ + a^\dagger \sigma_{e2A}^-) + \hbar g_{e2B} (a \sigma_{e2B}^+ + a^\dagger \sigma_{e2B}^-), \quad (3)$$

where a^\dagger and a are photon creation and annihilation operators, σ^+ and σ^- are the raising and lowering operators of the TLS excitons, and the rest of the notation is the same as in Eq. (2). The Hamiltonian in Eq. (3) is built in rotating wave approximation, which means that transition frequencies of TLS systems must be close to the cavity resonant frequency. This condition allows us to neglect fast-oscillating terms in the Hamiltonian but imposes restrictions on the frequency range: $|\omega_c - \omega_e| \ll |\omega_c + \omega_e|$. Also, to simplify the model, we do not consider direct exciton-exciton interaction. This assumption is justified by the detuned excitonic resonances and the rapid decay of dipole-dipole interaction with distance [9,29]. Thus, the energy exchange between excitons is provided only by the cavity photons. It is worth noting that we consider the single-photon manifold, which is valid under the weak driving conditions typically employed in experiments.

For the calculation of exciton population dynamics, we utilize a Lindblad master equation, which allows us to include losses without modifying the Hamiltonian and losing of the hermicity [30]. The Lindblad master equation is based on the density matrix formalism and for the considered system can be written in the following form:

$$\begin{aligned} \frac{\partial \rho}{\partial t} = & -\frac{i}{\hbar}[H, \rho] + \frac{\gamma_c}{2}\mathcal{L}[a]\rho + \frac{\gamma_{1A}}{2}\mathcal{L}[\sigma_{e1A}^-]\rho \\ & + \frac{\gamma_{2A}}{2}\mathcal{L}[\sigma_{e2A}^-]\rho + \frac{\gamma_{2B}}{2}\mathcal{L}[\sigma_{e2B}^-]\rho, \end{aligned} \quad (4)$$

where ρ is the density matrix of the full system, and $\mathcal{L}[A]\rho$ is a Lindbladian superoperator which is defined by the action on an arbitrary operator A as follows:

$$\mathcal{L}[A]\rho = 2A\rho A^\dagger - \rho A^\dagger A - A^\dagger A\rho. \quad (5)$$

The density matrix obtained from Eq. (4) can be used to find the time evolution of the average of physical quantities. Populations of the cavity photon and excitons are defined by the following formulas:

$$n_c(t) = \text{Tr}[\rho(t)a^\dagger a], \quad (6)$$

$$n_{1A}(t) = \text{Tr}[\rho(t)\sigma_{e1A}^+\sigma_{e1A}^-], \quad (7)$$

$$n_{2A}(t) = \text{Tr}[\rho(t)\sigma_{e2A}^+\sigma_{e2A}^-], \quad (8)$$

$$n_{2B}(t) = \text{Tr}[\rho(t)\sigma_{e2B}^+\sigma_{e2B}^-]. \quad (9)$$

V. RESULTS AND DISCUSSION

The energy exchange between excitons can be driven by their interaction with the cavity vacuum field, whose resonant frequency depends on the cavity length. When an exciton and the cavity field form a hybrid state, the excited exciton relaxes to the ground state through photon emission, and later on, it can be excited again by absorbing a photon. This energy exchange process repeats in time in cycles called Rabi oscillations. Figure 3 shows the experiment-based simulations of excitons and photon populations in our TMD cavity system as a function of time. First, we study the population dynamics of each TMD material coupled to the cavity field separately, and later, we study the combined system comprising both materials in the cavity. Figure 3(a) represents population

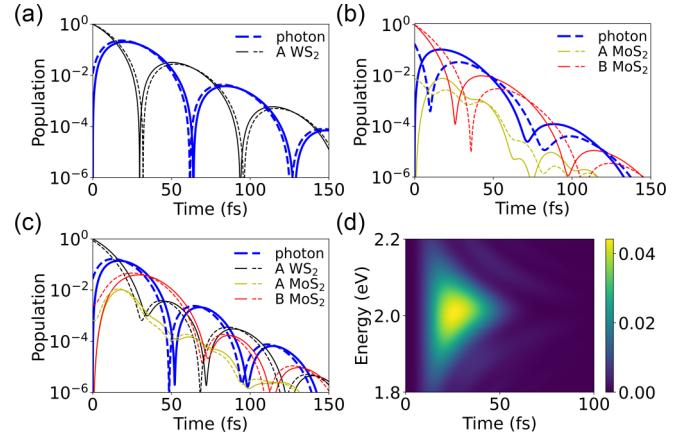


FIG. 3. Population dynamics of excitons in the optical cavity. (a)–(c) Simulation results calculated with a non-Hermitian Hamiltonian (dashed lines) and Lindblad master equation (solid lines): (a) WS₂ A exciton (black curves), (b) MoS₂ A [red (gray) curves] and B [olive (light gray) curves] excitons, (c) WS₂ A and MoS₂ A and B excitons. Blue thick curves denote cavity photon for all three figures. Parameters are taken from the Table I. Frequency of the cavity photon: (a) $\omega_c = \omega_{1A}$, (b) $\omega_c = \omega_{2B}$, and (c) $\omega_c = (\omega_{1A} + \omega_{2B})/2 = 2020$ meV. (d) Time-dependent total population of MoS₂ excitons vs frequency of the cavity photon.

oscillations of the initially excited WS₂ A exciton, which is strongly coupled to the microcavity (all parameters for this and further simulations are taken from Table I). The coincidence of the cavity mode and excitonic transition frequencies ($\omega_c = \omega_{1A} = 2019$ meV) provides the most efficient energy exchange.

The population dynamics in the MoS₂-cavity system is more complicated due to the presence of two exciton transitions able to exchange energy with the cavity field: A and B excitons. Figure 3(b) shows the population dynamics of MoS₂ A and B excitons in the microcavity. The plot shows that initially excited B exciton exchanges energy with the cavity and A exciton, although they are not coupled directly with the latter one. The A exciton oscillation amplitude is weak compared with the photon contribution to the exchange due to the neglect of exciton-exciton coupling and far detuning ($\omega_c = \omega_{2B} = 2021$ meV). It means that there is no significant energy exchange with the MoS₂ A exciton, and the contribution of the B exciton is dominant.

Figure 3(c) illustrates the population dynamics of the system of three excitons coupled to the microcavity and uncoupled from each other. The cavity resonant frequency $\omega_c = 2020$ meV is chosen between WS₂ A and MoS₂ B excitonic resonances. We consider the case when initially only the WS₂ exciton is excited (the case when the MoS₂ B exciton is initially excited has similar behavior and is presented in Appendix B). The result of the calculation shows that the system exhibits the essential energy exchange between WS₂ A and MoS₂ B excitons because of their close resonance frequencies. The efficiency of the transfer in this case reaches 4% with respect to the initial energy of the system, whereas the MoS₂ A exciton gives a smaller contribution to the exchange due to the reasons listed above and has a population maximum of $\sim 1\%$.

The efficiency of the exchange strongly depends on the cavity resonance frequency which allows us to tune the energy exchange between distant excitons. In Fig. 3(d), the time-dependent total population of MoS₂ excitons for different cavity frequencies (1.8–2.2 eV) is shown. From this plot, there is a maximum exchange efficiency which lies near resonances of WS₂ A and MoS₂ B excitons. In addition to the region where we can observe a clear exchange between considered excitons, there are two regions where the investigated ET is not pronounced: $\sim > 2.05$ and < 1.95 eV. In these regions, high detuning does not allow substantial energy exchange, and just straight decay of the excited WS₂ exciton prevails. Weak oscillations, expressed by the low-intensity stripes, are basically due to the exchange of the excitons with the field.

ET efficiency between WS₂ and MoS₂ A excitons is low compared with WS₂ A exciton and MoS₂ B exciton exchange. However, it is noteworthy that the exchange between these two excitons is nontrivial because of the more general nonresonant case which can occur in our system with two different materials (the frequencies of these two excitonic transitions are noticeably separated). If considering the exchange only between these two far-detuned excitons, the transfer efficiency has a maximum that corresponds to the cavity photon frequency between the considered excitonic transitions: $\omega_c^{\max} = (\omega_{1A} + \omega_{2A})/2 \approx 1.95$ eV. The MoS₂ A exciton population dynamics can be found in Appendix B.

VI. CONCLUSIONS

Our results suggest the existence of ultrafast long-distance ET between excitons in the WS₂ heterostructure and MoS₂ bilayer in a tunable microcavity. The coherent ET between these excitons results in the formation of exciton-polaritons in the strongly coupled regime. We have shown that polariton-assisted exciton population exchange dynamics can occur over 1 μm distance between the interacting materials. Our calculations show that the most efficient energy exchange between excitons can be observed when the cavity frequency lies near excitonic transition frequencies in the resonant ET case and between the donor and acceptor resonant frequencies in the nonresonant ET case. Due to the damping processes, the first cycle of the exchange population dynamics is the most pronounced and can be observed at ~ 30 fs from the starting point.

The results of this paper can be used in future experimental realizations of similar polaritonic systems. Modern state-of-the-art techniques already operate with a high temporal resolution which allows us to resolve ultrafast Rabi oscillations [31]. It convinces us that our work brings the appearance of stable RT quantum devices highly desirable for modern technologies closer.

ACKNOWLEDGMENTS

This paper was supported by the Academy of Finland (Grants No. 314810, No. 332743, No. 333982, No. 336144, No. 352780, No. 352930, and No. 353364), the Academy of Finland Flagship Programme (Grant No. 320167, PREIN), the EU H2020-MSCA-RISE-872049 (IPN-Bio), the Jane and Aatos Erkkö Foundation and the Technology Industries of Finland Centennial Foundation (Future Makers 2022), and

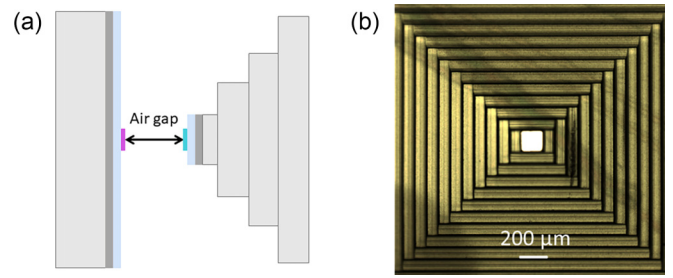


FIG. 4. (a) Schematic picture of side view of the open cavity system and (b) microscope image of the top view of pyramid-shaped small mirror forming the right side of the cavity. The mirror area can be seen as a bright area in the middle.

the ERC (Grant No. 834742). We acknowledge the provision of facilities by Aalto University at OtaNano—Micronova Nanofabrication Centre.

T.P. and F.N. contributed equally to this paper.

APPENDIX A: THE STRUCTURE AND ALIGNMENT OF AN OPEN CAVITY

The structure of the free-space cavity setup is presented in Fig. 4(a), and a microscope image of the smaller mirror is presented in Fig. 4(b). The larger mirror was deposited on a 1×1 cm chip cut from 4'' silica wafer. One cavity mirror was cut to have a small contact area with another mirror, as seen in Fig. 4(a). This allows the cavity to achieve shorter cavity lengths since an open-cavity structure such as this will always have some misalignment.

The smaller mirror was produced from a chip identical to the larger mirror by using a wafer dicing saw (DAD3220 by DISCO Corporation). The sides of the pyramid shape were produced by cutting gradually deeper cuts to the chip while moving it sideways in 50 μm intervals between each cut, leaving the mirror area at the apex of the pyramid at $\sim 150 \times 150 \mu\text{m}$ and the base area of the pyramid at $\sim 3 \times 3$ mm. The MoS₂ bilayer was transferred to the mirror after the cutting process.

The cavity mirrors were aligned by using interference fringes in the cavity transmission spectra. The cavity was illuminated by monochromatic light, and the interference fringes were eliminated by tuning the mirror tilt angles. After tuning, the air gap of the cavity could be reduced to 700 nm until the mirrors started to touch from one corner due to small misalignment.

The cavity length and thus the order of the cavity mode were determined by calculating transmission spectra as a function of air gap that fit the measured data. The inclination of cavity modes changes from more horizontal to more vertical as the cavity length increases. The proper fit is determined by comparing calculated cavity modes as a function of air gap to measured cavity modes as a function of the piezovoltage. The comparison of these mappings has consistently only one proper fit, so the piezovoltage axis of the measurement can be accurately converted to air gap in nanometers. A cavity decay rate was determined from the full width at half maximum of the empty cavity transmission spectrum.

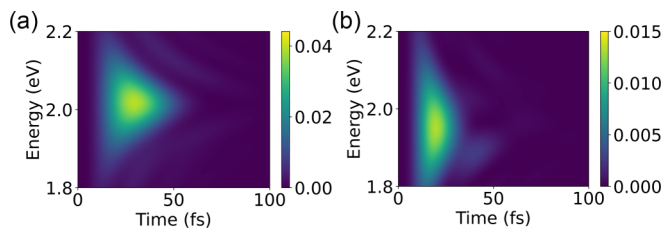


FIG. 5. (a) WS₂ A exciton population dynamics when MoS₂ B exciton is initially excited. (b) Population dynamics of MoS₂ A exciton when WS₂ A exciton is initially excited (nonresonant exchange).

APPENDIX B: EXCITON POPULATION DYNAMICS SIMULATIONS

Figure 5(a) illustrates time-dependent population dynamics of the WS₂ A exciton when the MoS₂ B exciton is initially excited. Despite the insignificant differences with Fig. 3(d), the general behavior of the exchange stays the same. The case of the ET between WS₂ and MoS₂ A excitons has lower

transfer efficiency but is of interest because of the nonresonant nature of the process. Despite the large detuning, ET still occurs, as seen from Fig. 5(b), where the MoS₂ A exciton population dynamics is presented. The maximum of the transfer efficiency in this case corresponds to the cavity frequency between frequencies of the considered excitons and equals 1.95 eV at ~ 20 fs.

The results of the calculations obtained with an analytical non-Hermitian Hamiltonian approach [dashed lines in Figs. 3(a)–3(c)] and with the Lindblad master equation using QuTiP [32] (solid lines) match very well for the considered parameters of the system. Minor misalignment arises from the non-hermicity of the Hamiltonian in the first approach, which can still describe the dynamics of the system with sufficient precision from the experimental point of view. The most significant and systematic difference is near the starting point ($t = 0$): a non-Hermitian Hamiltonian gives us a nonzero population, even for states that are supposed to be nullified. This drawback of the method is not crucial for the case of the sufficiently small decay rates.

- [1] D. Sanvitto and S. Kéna-Cohen, The road towards polaritonic devices, *Nat. Mater.* **15**, 1061 (2016).
- [2] M. A. Castellanos, A. Dodin, and A. P. Willard, On the design of molecular excitonic circuits for quantum computing: The universal quantum gates, *Phys. Chem. Chem. Phys.* **22**, 3048 (2020).
- [3] T. C. H. Liew and Y. G. Rubo, Quantum exciton-polariton networks through inverse four-wave mixing, *Phys. Rev. B* **97**, 041302(R) (2018).
- [4] B. Guzelturk and H. V. Demir, Near-field energy transfer using nanoemitters for optoelectronics, *Adv. Funct. Mater.* **26**, 8158 (2016).
- [5] T. Förster, Zwischenmolekulare Energiewanderung und Fluoreszenz, *Ann. Phys.* **437**, 55 (1948)
- [6] F. Benimetskiy, A. Yulin, A. Mikhin, V. Kravtsov, I. Iorsh, M. Skolnick, I. Shelykh, D. Krizhanovskii, and A. Samusev, Non-linear self-action of ultrashort guided exciton-polariton pulses in dielectric slab coupled to 2D semiconductor, *2D Mater.* **10**, 045016 (2023).
- [7] D. M. Coles, N. Somaschi, P. Michetti, C. Clark, P. G. Lagoudakis, P. G. Savvidis, and D. G. Lidzey, Polariton-mediated energy transfer between organic dyes in a strongly coupled optical microcavity, *Nat. Mater.* **13**, 712 (2014).
- [8] X. Zhong, T. Chervy, S. Wang, J. George, A. Thomas, J. A. Hutchison, E. Devaux, C. Genet, and T. W. Ebbesen, Non-radiative energy transfer mediated by hybrid light-matter states, *Angew. Chem., Int. Ed.* **55**, 6202 (2016).
- [9] M. Ściesiek, K. Sawicki, W. Pacuski, K. Sobczak, T. Kazimierzczuk, A. Golnik, and J. Suffczyński, Long-distance coupling and energy transfer between exciton states in magnetically controlled microcavities, *Commun. Mater.* **1**, 78 (2020).
- [10] K. Georgiou, R. Jayaprakash, A. Othonos, and D. G. Lidzey, Ultralong-range polariton-assisted energy transfer in organic microcavities, *Angew. Chem. Int. Ed.* **60**, 16661 (2021).
- [11] C. R. Kagan, L. C. Bassett, C. B. Murray, and S. M. Thompson, Colloidal quantum dots as platforms for quantum information science, *Chem. Rev.* **121**, 3186 (2021).
- [12] A. P. Demchenko, Photobleaching of organic fluorophores: Quantitative characterization, mechanisms, protection, *Methods Appl. Fluoresc.* **8**, 022001 (2020).
- [13] E. Jung, J. C. Park, Y. S. Seo, J. H. Kim, J. Hwang, and Y. H. Lee, Unusually large exciton binding energy in multilayered 2H-MoTe₂, *Sci. Rep.* **12**, 4543 (2022).
- [14] J. Gu, B. Chakraborty, M. Khatoniar, and V. M. Menon, A room-temperature polariton light-emitting diode based on monolayer WS₂, *Nat. Nanotechnol.* **14**, 1024 (2019).
- [15] X. Liu, T. Galfsky, Z. Sun, F. Xia, E.-c. Lin, Y.-H. Lee, S. Kéna-Cohen, and V. M. Menon, Strong light-matter coupling in two-dimensional atomic crystals, *Nat. Photon.* **9**, 30 (2015).
- [16] H. Shan, L. Lackner, B. Han, E. Sedov, C. Rupprecht, H. Knopf, F. Eilenberger, J. Beierlein, N. Kunte, M. Esmann *et al.*, Spatial coherence of room-temperature monolayer WSe₂ exciton-polaritons in a trap, *Nat. Commun.* **12**, 6406 (2021).
- [17] M. Amani, D.-H. Lien, D. Kiriya, J. Xiao, A. Azcatl, J. Noh, S. R. Madhupathy, R. Addou, S. KC, M. Dubey *et al.*, Near-unity photoluminescence quantum yield in MoS₂, *Science* **350**, 1065 (2015).
- [18] G.-H. Lee, X. Cui, Y. D. Kim, G. Arefe, X. Zhang, C.-H. Lee, F. Ye, K. Watanabe, T. Taniguchi, P. Kim *et al.*, Highly stable, dual-gated MoS₂ transistors encapsulated by hexagonal boron nitride with gate-controllable contact, resistance, and threshold voltage, *ACS Nano* **9**, 7019 (2015).
- [19] N. Lee and H. Jeon, Role of an Al₂O₃ passivation layer during annealing of 2D-SnS₂ thin films grown by atomic layer deposition, *ECS J. Solid State Sci. Technol.* **10**, 023001 (2021).
- [20] L. C. Flatten, Z. He, D. M. Coles, A. A. Trichet, A. W. Powell, R. A. Taylor, J. H. Warner, and J. M. Smith, Room-temperature exciton-polaritons with two-dimensional WS₂, *Sci. Rep.* **6**, 33134 (2016).
- [21] W. Xu, D. Kozawa, Y. Zhou, Y. Wang, Y. Sheng, T. Jiang, M. S. Strano, and J. H. Warner, Controlling photoluminescence enhancement and energy transfer in WS₂ : hBN : WS₂ vertical stacks by precise interlayer distances, *Small* **16**, 1905985 (2020).

- [22] S. Wang, Q. Le-Van, F. Vaianella, B. Maes, S. E. Barker, R. H. Godiksen, A. G. Curto, and J. Gomez Rivas, Limits to strong coupling of excitons in multilayer WS₂ with collective plasmonic resonances, *ACS Photonics* **6**, 286 (2019).
- [23] A. Castellanos-Gomez, M. Buscema, R. Molenaar, V. Singh, L. Janssen, H. S. J. van der Zant, and G. A. Steele, Deterministic transfer of two-dimensional materials by all-dry viscoelastic stamping, *2D Mater.* **1**, 011002 (2014).
- [24] S. Puebla, H. Li, H. Zhang, and A. Castellanos-Gomez, Apparent colors of 2D materials, *Adv. Photonics Res.* **3**, 2100221 (2022).
- [25] J. Hopfield, Theory of the contribution of excitons to the complex dielectric constant of crystals, *Phys. Rev.* **112**, 1555 (1958).
- [26] G. Khitrova, H. Gibbs, M. Kira, S. W. Koch, and A. Scherer, Vacuum Rabi splitting in semiconductors, *Nat. Phys.* **2**, 81 (2006).
- [27] M.-A. Miri and A. Alù, Exceptional points in optics and photonics, *Science* **363**, eaar7709 (2019).
- [28] E. T. Jaynes and F. W. Cummings, Comparison of quantum and semiclassical radiation theories with application to the beam maser, *Proc. IEEE* **51**, 89 (1963).
- [29] W. Zhang, J. B. You, J. Liu, X. Xiong, Z. Li, C. E. Png, L. Wu, C. W. Qiu, and Z. K. Zhou, Steering room-temperature plexcitonic strong coupling: A diexcitonic perspective, *Nano Lett.* **21**, 8979 (2021).
- [30] F. Roccati, G. M. Palma, F. Ciccarello, and F. Bagarello, Non-Hermitian physics and master equations, *Open Syst. Inf. Dyn.* **29**, 2250004 (2022).
- [31] L. Dominici, D. Colas, S. Donati, J. P. Restrepo Cuartas, M. De Giorgi, D. Ballarini, G. Guirales, J. C. López Carreño, A. Bramati, G. Gigli *et al.*, Ultrafast control and Rabi oscillations of polaritons, *Phys. Rev. Lett.* **113**, 226401 (2014).
- [32] J. Johansson, P. Nation, and F. Nori, QuTiP 2: A Python framework for the dynamics of open quantum systems, *Comput. Phys. Commun.* **184**, 1234 (2013).